Suprathermal electron transport studies in radio-frequency-heated tokamak plasmas

Jean Cazabonne[1,*], *Tullio* Barbui[2], *Stefano* Coda[3], *Joan* Decker[3], *Ewout* Devlaminck[3], *Peter* Donnel[1], *Rémi* Dumont[1], *Annika* Ekedahl[1], *Théo* Fonghetti[1], *Pierre* Forestier-Colleoni[1], *Pierre* Manas[1], *Didier* Mazon[1], *Samuele* Mazzi[1], *Rémy* Nouailletas[1], *Xavier* Regal-Mezin[1], *Riccardo* Saura[1], *Yves* Savoye-Peysson[1], the TCV Team[3,**], and the WEST Team[1,***]

[1]CEA, IRFM, F-13108 Saint-Paul-lez-Durance, France
[2]Princeton Plasma Physics Laboratory, Princeton, NJ 08540, United States of America
[3]École Polytechnique Fédérale de Lausanne (EPFL), Swiss Plasma Center (SPC), CH-1015 Lausanne, Switzerland

Abstract. This contribution reports on the study of suprathermal electron radial transport enhancement in the presence of electron-heating radio-frequency waves, such as electron-cyclotron waves or lower-hybrid waves. Since suprathermal electrons emit hard X-rays from Bremsstrahlung, experimental data from hard X-ray measurements are used to follow their dynamics. In particular, electron-cyclotron power modulation experiments performed in TCV show that this transport depends on the total electron-cyclotron power. These results are corroborated by experimentally constrained Fokker-Planck simulations [J. Cazabonne et al, Plasma Phys. Control. Fusion **65**, 104001 (2023)]. Similar experiments have been performed in WEST with lower-hybrid waves, and are reported for the first time. Preliminary analyses show potential evidence of suprathermal electron transport, but no clear dependence on wave power nor photon energy at this stage.

1 Introduction

Radio-Frequency (RF) waves are routinely launched in tokamak plasmas to drive current by accelerating electrons to suprathermal energies. Different ranges of frequencies are used to achieve different objectives. High frequency Electron-Cyclotron (EC) waves benefit from their ability to drive a highly localized current density to tailor the plasma current profile, thus enabling the control and the mitigation of magneto-hydro-dynamic instabilities to improve the plasma stability. On the other hand, the lower frequency Lower-Hybrid (LH) waves are one of the main choices for efficiently driving and sustaining non-inductive current, enabling the exploration of long-pulse operation in today's tokamaks, such as in EAST or WEST [1].

However, it is far from straightforward to experimentally characterize the power deposition profile and the associated current density. This heavily relies on simulations, from integrated modelling using simplified models for the wave-plasma interaction to more sophisticated quasilinear drift-kinetic Fokker-Planck models. Even these Fokker-Planck models suffer from the lack of first principles turbulent transport calculation, and the matching of the simulated data with the experimental ones requires the addition of ad-hoc radial transport of suprathermal electrons, ranging between 1 and 4 m^2/s for EC waves [2–4] and 0.1 and 0.3 m^2/s for the LH waves [5].

For LH waves in Alcator C-Mod, only 0.02 m^2/s of maximum diffusion coefficient and 0.75 m/s of maximum convection velocity are measured, consistent with Fokker-Planck simulations [6]. On the other hand, in Tore Supra, LH power-modulation experiments have also shown that the increase of core temperature caused by the waves is delayed in time with respect to the applied LH power, highlighting a potential inward heat transport. Explaining this transport involving only the anomalous radial transport of suprathermal electrons leads to high values of diffusion coefficients (10 m^2/s), compatible with turbulent transport from small magnetic field fluctuations ($\delta B/B \sim 10^{-4}$) [7]. Still in Tore Supra, using LH waves, a radial diffusion time of the suprathermal electron of 2 ± 1 s has been estimated [8].

This contribution reports on power-modulation experiments performed to investigate the radial transport of suprathermal electrons, using the hard X-rays (HXR) as a signature for their spatial distribution, energy and density. From these perturbative studies, it is possible to estimate a radial diffusion of these electrons [9]. This method has been applied in the TCV tokamak for the EC waves [3, 4]. For the LH waves, power-modulation experiments are performed in the WEST tokamak.

Section 2 is dedicated to the experimental setup and plasma scenario used to estimate the radial diffusion of suprathermal electrons in both machines. Section 3 details the experimental characterization of the suprathermal electron transport performed in TCV for the EC waves, while 4 reports on the preliminary estimation of this transport for LH waves, performed in WEST for the first time.

*Corresponding author: jean.cazabonne@cea.fr
See author list of B.P. Duval et al, Nuclear Fusion **64, 112023 (2024)
***See http://west.cea.fr/WESTteam

Section 5 concludes this study and provides outlooks on the forthcoming analyses.

2 Experimental setup and scenarios for suprathermal electron transport characterization

Both EC current drive (ECCD) and LH current drive (LHCD) generate a population of suprathermal electrons, but the power deposition profile in phase space can be very different for the two mechanisms. This may lead to different dynamics (generation, transport, relaxation) of the so-generated suprathermal electron population. A key difference between LHCD and ECCD is illustrated in Figures 1 and 2. They show that the main lobe of the LH $N_\parallel$-spectrum (where $N_\parallel$ is the parallel refractive index with respect to the background magnetic field) undergoes multiple-pass absorption, potentially leading to a broader power deposition profile than the ECCD, which on the contrary undergoes efficient single-pass absorption. The absorption mechanism itself plays a major role in the localization of the power deposition profile. EC waves resonates with a thin layer of the plasma around a given value of the magnetic field [10], while LH waves are Landau damped over a wider range, as soon as the electron temperatures is high enough. For a given $N_\parallel$, the strong Landau damping condition reads $T_e[\text{keV}] \simeq 42.25/N_\parallel^2$ [11]. In practice, the LH $N_\parallel$-spectrum has more than one lobe, and different wave-plasma interaction mechanisms are expected to upshift the $N_\parallel$-spectrum in the scrape-off layer (SOL) [12]. The accurate determination of the LH power deposition profile is therefore challenging, as it is very sensitive to the type of model used to described the coupled LH spectrum. But, overall, it is expected to be broader than the EC power deposition profile.

2.1 Main Hard X-Ray diagnostics

In tokamaks, electrons accelerated to suprathermal energies by their interaction with externally launched waves emit hard X-rays from Bremsstrahlung. It is therefore possible to follow their dynamics by measuring those hard X-rays. The main technique used in this study relies on compact solid-state cadmium-telluride photo-diodes, which can probe photons ranging between 20 keV and 200 keV. In WEST, a 38-diodes pinhole camera looking at the poloidal section is installed on the low-field side since Tore Supra era, mentioned hereafter as DVSPX [13]. A Multi-Energy Hard X-Ray camera (ME-HXR), based on a 487×195 pixelated cadmium-telluride sensor, is also installed in WEST [14], but the analysis of its data is left for future work. On the other hand, TCV is equipped with four tungsten-shielded 25-diodes cameras with collimated lines of sight covering a poloidal section of the plasma [15], later referred to as HXRS. The lines of sight of these diagnostics are displayed in Figures 1 and 2.

2.2 Plasma scenario and conditional averaging

One way to study the dynamics of the suprathermal electrons is to perform modulations of the source of these suprathermal electrons, i.e. modulations of the EC or the LH power. The idea is to locally perturb the population of suprathermal electrons, without affecting the background plasma too much, and to study the propagation of this perturbation. To minimize the disturbance of the plasma caused by the power modulations, the duration of the high-power phase of the modulation cycle τ_{HP} is set such that $\tau_{HP} \ll \tau_{D,J}$, where $\tau_{D,J}$ is the current diffusion time, as defined in [3, 16]. Typically, for the discharges presented in this paper, $\tau_{D,J}$ is of the order of few tens of milliseconds to a hundred of milliseconds for ECCD in TCV [4]

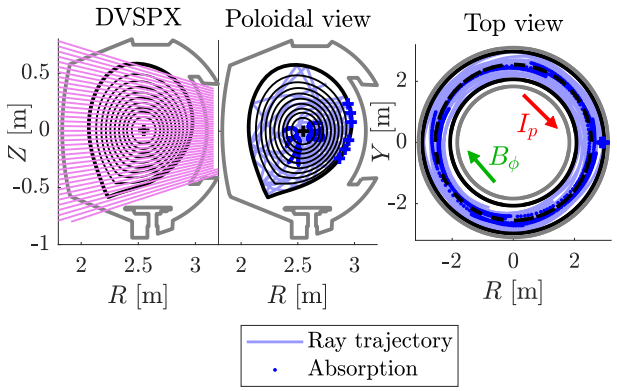

Figure 1. DVSPX lines of sight displayed on a poloidal section of WEST (*left*). Co-current LHCD ray propagation in WEST (3.7 GHz slow wave with $N_\parallel = -2$ corresponding to the main lobe, WEST shot #62002) displayed on a poloidal section (*middle*) and on a top view (*right*). On the top view, the wave is propagating counter-clockwise, undergoing multiple-pass absorption. Ray propagation and absorption computed by C3PO.

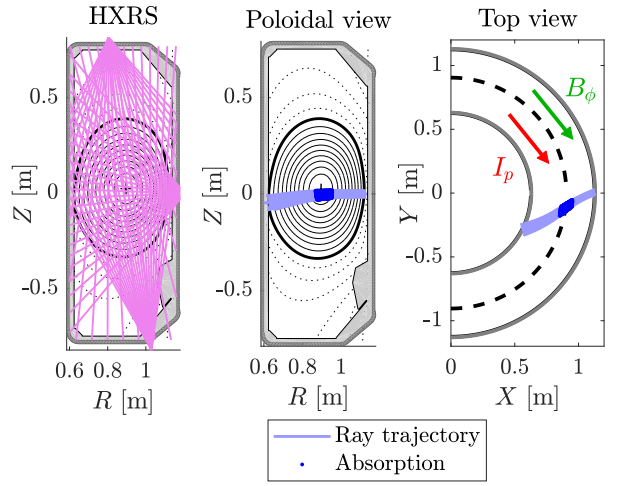

Figure 2. HXRS lines of sight displayed on a poloidal section of TCV (*left*). Counter-current ECCD beam propagation in TCV (82.7 GHz X2 beam with $N_\perp/N_\parallel = \tan(57^o)$, TCV shot #74304) displayed on a poloidal section (*middle*) and on a top view (*right*). Ray propagation and absorption computed by C3PO.

and it ranges between few hundreds of milliseconds and a second for LHCD in WEST. On the other hand, the time between the power pulses τ_{LP} needs to be sufficiently long for the suprathermal electron to relax, which translates by $\tau_{LP} \sim \tau_{SL}^{sup.e}$ where $\tau_{SL}^{sup.e}$ is the collisional slowing-down time of the suprathermal electrons on bulk electrons.

This results in rather short power modulation cycles with respect to the temporal resolution of the diagnostics. Typically, in TCV, EC pulses are 11-ms long, with $\tau_{HP} = 2$ ms. The HXRS is setup with a 0.2 ms integration time to resolve the EC power modulation cycles, but the number of photons collected over this short time period is very low, leading to a poor signal-to-noise ratio. This is illustrated in the top-left corner of Figure 3. To overcome this difficulty, the HXRS signal is averaged over the 48 power modulation cycles, increasing the photon statistics, as shown in the bottom-left corner of Figure 3. This conditional averaging assumes that all the power modulation cycles are physically identical. As shown in Figure 2, the EC beam is launched in the equatorial mid-plane. This setup helps to minimize the effect of beam broadening, caused by the scattering off edge turbulent structures, on the power deposition profile [17]. The list of TCV shots used in this study is given in Table 1.

Table 1. TCV shot list for the present study [4].

Shot #	$N_\perp/N_\parallel$	ΔP_{EC}	Background P_{EC}
#74304	tan (57^o)	589 kW	140 kW
#74310	tan (57^o)	589 kW	934 kW^a
#74305	tan (65^o)	589 kW	140 kW
#74309	tan (65^o)	589 kW	934 kW^a

^{a}140 kW in ECCD and 794 kW in pure ECRH ($N_\parallel = 0$) using a second EC launcher.

In WEST, LH pulses are 61-ms long, with $\tau_{HP} = 16$ ms. However, the DVSPX integration time is limited to 16 ms. Therefore, before the conditional averaging, data are smoothed by evenly spreading the number of photons collected over 16 ms into 16 bins of 1 ms, resulting in an artificial 1-ms time resolution. The initial temporal resolution of the DVSPX is illustrated in the top-right corner of Figure 3 and the conditional averaging of the smoothed data over 161 power modulation cycle is displayed in the bottom-right corner of Figure 3. The list of WEST shots used in this study is given in Table 2.

Table 2. WEST shot list for the present study. The LH power is evenly split between the two LH launchers of WEST, which have different phasing, i.e. different main $N_\parallel$ lobes.

Shot #	Main $N_\parallel$	ΔP_{LH}	Background P_{LH}
#62002	-2 / -1.8	1.0 MW	2.0 MW
#62004	-2 / -1.8	1.5 MW	2.0 MW
#62005	-2 / -1.8	2.0 MW	2.0 MW

2.3 Wave-plasma interaction modelling

The EC and LH wave power depositions are calculated with the 3D bounce-averaged drift-kinetic Fokker-Planck code LUKE [18], coupled to the ray-tracing code C3PO [19]. For WEST simulations, the equilibrium and profiles are calculated by the METIS code [20], based on experimental data. The coupled LH spectrum is calculated with ALOHA [21]. For TCV, the equilibrium is directly extracted from LIUQE reconstruction [22], using experimental profiles. Frozen-current time-dependent simulations have been performed for the EC waves in TCV and are reported in [4], but not yet for the LH waves in WEST (out of the scope of the present paper). Simulations are experimentally constrained by the total plasma current (without the bootstrap contribution) and by the HXR data. The HXR profiles and spectra are directly compared with results from the Bremsstrahlung calculation performed with R5X2 [23], using the electron distribution calculated by LUKE.

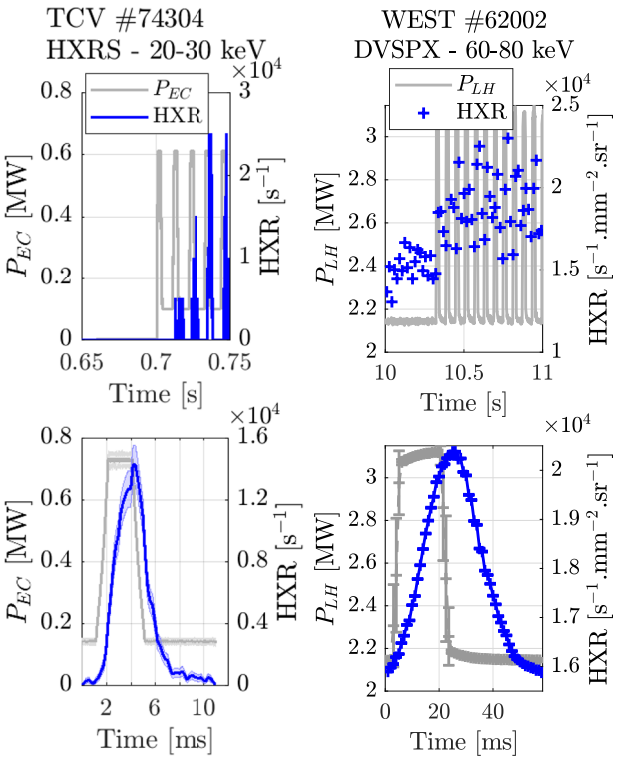

Figure 3. Examples of HXR time traces measured in TCV (*left column*) and in WEST (*right column*). Conditionally averaged data associated with 48 power modulation cycles in TCV and 161 power modulation cycles in WEST (*bottom row*).

3 Transport characterization for the EC waves in TCV

The propagation of the HXR perturbation is analyzed by tomographically inverting the conditionally averaged HXRS data, yielding a 2D HXR emissivity $\epsilon_{HXR}(\rho, \theta, t)$. The 1D emissivity profile is taken along the low-field side equatorial mid-plane, where the EC beam propagates: $\epsilon_{HXR}(\rho, t) \equiv \epsilon_{HXR}(\rho, \theta = 0, t)$ (throughout this paper, ρ is defined as the square root of the normalized poloidal magnetic flux). The resulting emissivity time traces at each location are then smoothed using a moving average

with a 7-samples-wide window. From the time-dependent 1D emissivity profiles, it is possible to perform a phase-amplitude analysis of the HXR perturbation. The delay in the HXR rising front is estimated by computing the cross-correlation $c_\times$ between the normalized emissivity at the EC wave absorption location $\bar{\epsilon}_{HXR}(\rho_{abs}, t)$, and the normalized emissivity at every other location. It reads

$$c_\times(\rho, \tau) = \int_{-\infty}^{+\infty} \bar{\epsilon}_{HXR}(\rho_{abs}, t)\bar{\epsilon}_{HXR}(\rho, t-\tau)\mathrm{d}t\,, \quad (1)$$

where the actual delay at each location $\tau_d(\rho)$ is found by taking the maximum of $c_\times$ at each ρ. This delay in the HXR rising front from the wave absorption location is associated with the phase of the HXR perturbation. The amplitude of the perturbation is found by taking the non-normalized emissivity associated with the delay $\epsilon^*_{HXR}(\rho) \equiv \epsilon_{HXR}(\rho, \tau_d)$. The phase velocity $v_{\phi,d}$ and the decay length λ_d of the perturbation are estimated from the following fits

$$\tau_d(r) = v_{\phi,d}^{-1} r + \tau_{d,0}\,, \quad (2)$$

$$\ln(\epsilon^*_{HXR})(r) = \lambda_d^{-1} r + \ln(\epsilon^*_{HXR})_0\,, \quad (3)$$

where r is the minor radius coordinate. The radial diffusion coefficient can then be estimates as $D_r = v_{\phi,d}\lambda_d/2$ [9]. This analysis process is illustrated in Figure 4.

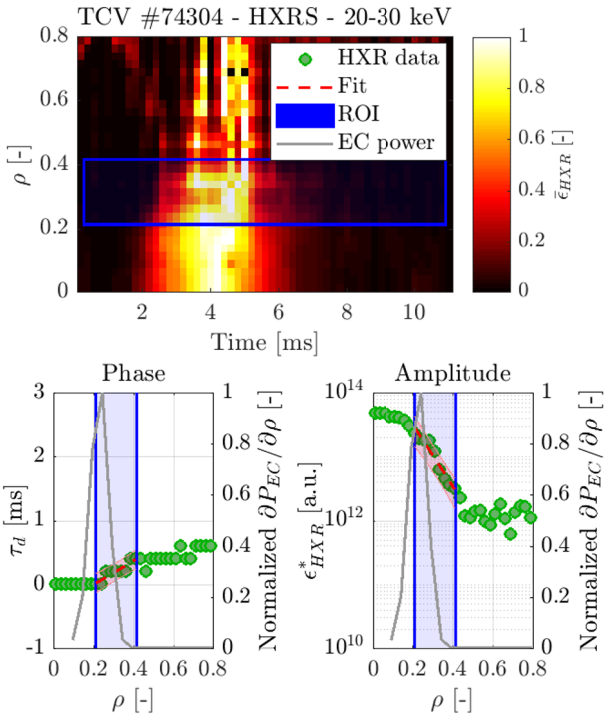

Figure 4. Phase-amplitude analysis for TCV shot #74304. 2D map of normalized HXR emissivity (*top*). The range of interest (ROI) for the fits is highlighted in blue. Phase (*bottom-left*) and amplitude (*bottom-right*) with the EC power deposition profile computed with LUKE overlaid in grey.

Results are shown in Figure 5 for the TCV shots presented in Table 1. The radial diffusion of the HXR perturbation, associated with the transport of suprathermal electrons, increases with the background EC power, while no clear effect of $N_\parallel$ is evidenced. These results are consistent with experimentally constrained LUKE simulations of the same shots, in which the ad-hoc model for the radial diffusion operator is chosen to be proportional to the wave diffusion operator, meaning that it only acts on suprathermal electrons interacting with the EC wave. The amplitude of this radial diffusion operator is controlled by a coefficient D_{r0}, which is plotted in Figure 5. An in-depth analysis of these results is found in [4].

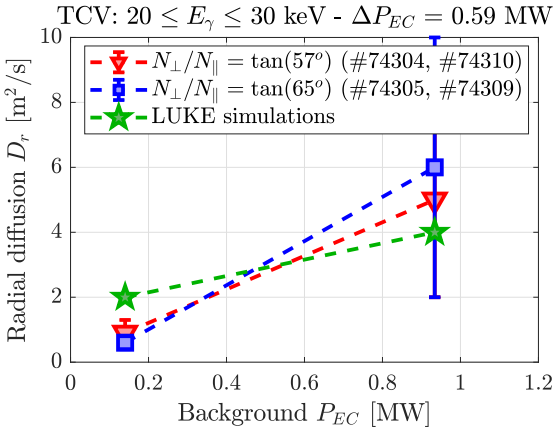

Figure 5. Experimental diffusion coefficient for the suprathermal electrons in TCV using ECCD, estimated from the HXRS data taken between 20 and 30 keV. D_{r0} from experimentally constrained LUKE simulations is overlaid.

4 Preliminary transport characterization for the LH waves in WEST

A preliminary analysis of the suprathermal electron transport is proposed for LH waves in WEST. Two major differences from the analysis done in TCV have to be highlighted. First, a proper Abel inversion of the DVSPX data has not been performed yet, and a simple projection of the line-integrated DVSPX measurements on the vertical axis Z, at a major radius $R = 2.5$ m has been used. It has to be noticed that, since only one DVSPX camera is installed on WEST (see Figure 1), no advanced 2D tomography including poloidal asymmetry can be performed.

The other main difference is that no cross-correlation is used to estimate the delay in the HXR rising front. Instead, the HXR rising time is estimated from the normalized HXR count rate $\bar{I}_{HXR}(t)$ at each location Z, by taking the average time t_{rise} at which the signal rise from 0.9 to 1.0. The delay at each location τ_d is estimated by $\tau_d(Z) = t_{rise}(Z) - \min(t_{rise}(Z))$. The amplitude of the perturbation is calculated by taking the non-normalized HXR count rate at the rising time $I_{HXR}(Z) \equiv I_{HXR}(Z, t_{rise})$. Then, the phase velocity and the decay length of the perturbation are deduced from equations 2 and 3 respectively, replacing r by Z and ϵ^*_{HXR} by I_{HXR}. Such an analysis is illustrated in Figure 6.

This simplified analysis only provides a qualitative value of the diffusion coefficient rather than a quantitative value. Results are shown in Figure 7 for the WEST shots

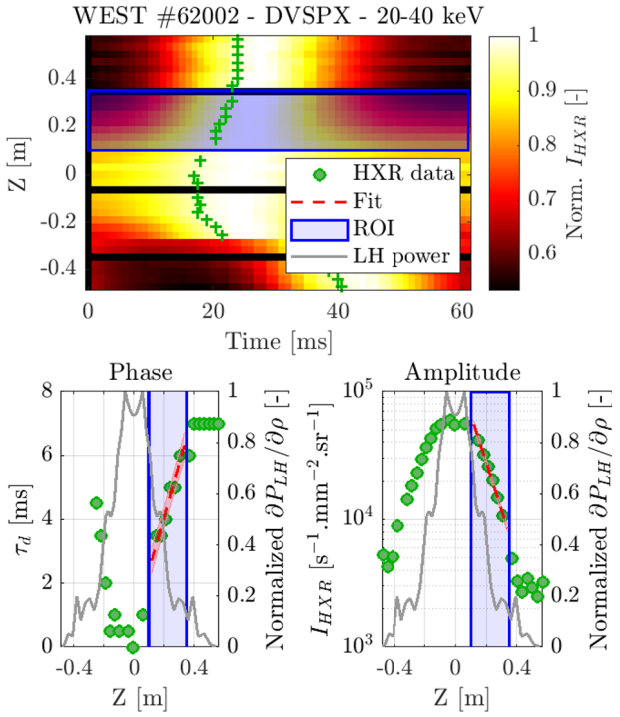

Figure 6. Phase-amplitude analysis for WEST shot #62002. 2D map of normalized HXR count rate with t_{rise} overlaid as green crosses (*top*). The range of interest (ROI) for the fits is highlighted in blue. Phase (*bottom-left*) and amplitude (*bottom-right*) with the LH power deposition profile computed with LUKE overlaid in grey.

listed in Table 2. It shows potential evidence of suprathermal electron transport with the LH waves, but no clear dependence are found on the photon energy nor on the power modulation amplitude. The absolute level, roughly ranging between 2 and 8 m^2/s, is significantly higher than the level usually admitted for LH waves [5, 6], but could be consistent with the explanations from [7], summarized in section 1. It has to be noticed that an absolute experimental characterization of the suprathermal electron diffusion for LH waves is challenging, since the power deposition profile is broader than for the EC waves (an example can be seen by comparing the power deposition profiles from Figures 4 and 6). This means that it is complicated to find a localization in the plasma free from the external power source over which the perturbation freely propagates. In other words, it may be difficult to disentangle the effect of heating and the different transport mechanisms at play in such a configuration. Moreover, the simplifications used to derive the experimental radial diffusion coefficient of the suprathermal electrons do not allow to draw quantitative conclusions at this stage.

5 Conclusions and outlooks

The experimental diffusion of suprathermal electron in presence of EC waves has already been compared in great details against simulations in [4]. In particular, it has been shown that the level of diffusion needed in forward

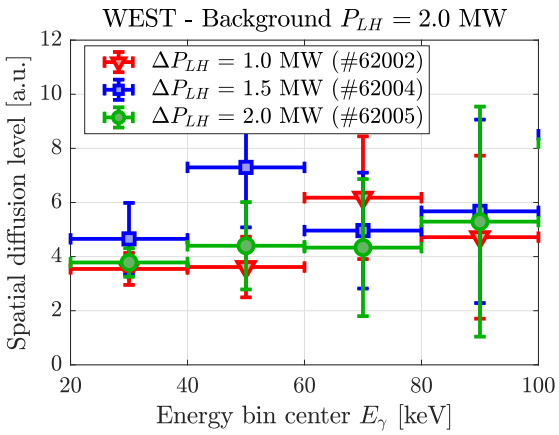

Figure 7. Experimental diffusion coefficient for the suprathermal electrons in WEST using LHCD, estimated from the DVSPX data taken between 20 and 100 keV.

drift-kinetic Fokker-Planck simulations performed with C3PO/LUKE/R5X2 to reproduce the HXR emission is coherent with the experimental level. Complementary studies presented in [4] show that, experimentally, turbulence seems to consistently increase with the EC power, which is corroborated by preliminary flux-driven gyro-kinetic simulations including EC waves. This points in the direction of an increased turbulent transport with EC power, which may explain the observed increased transport of suprathermal electrons with total EC power.

For the LH waves, preliminary analyses found potential evidence of suprathermal electron transport occurring in presence of LH waves. However, no clear dependence on the modulation amplitude, nor on the photon energy, has been observed at this stage. Further analysis is foreseen, using proper Abel inversions of the HXR data. It is also planned to perform time-dependent experimentally-constrained drift-kinetic Fokker-Planck LUKE simulations in order to check the relevance of the value of the experimental diffusion coefficient. This is is out of the scope of the present paper. To complete this analysis, experimental characterization of the turbulence is available for the WEST shots listed in Table 2, from Doppler Back-Scattering diagnostic and divertor-embedded Langmuir probes, and will be analyzed in future work. Finally, heat transport can also be studied using the ECE diagnostic of WEST.

Acknowledgements

This work has been carried out within the framework of the EUROfusion Consortium, partially funded by the European Union via the Euratom Research and Training Programme (Grant Agreement No 101052200 — EUROfusion). The Swiss contribution to this work has been funded by the Swiss State Secretariat for Education, Research and Innovation (SERI). Views and opinions expressed are however those of the author(s) only and do not necessarily reflect those of the European Union, the European Commission or SERI. Neither the European Union nor the European Commission nor SERI can be held responsible for them.

References

[1] A. Ekedahl, C. Bourdelle, J.F. Artaud, J.M. Bernard, H. Bufferand et al., Development of long pulse RF heating and current drive for H-mode scenarios with metallic walls in WEST, AIP Conference Proceedings **1689**, 030013 (2015). https://doi.org/10.1063/1.4936478

[2] P. Nikkola, O. Sauter, R. Behn, S. Coda, I. Condrea et al., Modelling of the electron cyclotron current drive experiments in the TCV tokamak, Nuclear Fusion **43**, 1343 (2003). https://doi.org/10.1088/0029-5515/43/11/006

[3] D. Choi, S. Coda, J. Decker, J.A. Cazabonne, Y. Peysson, Study of suprathermal electron dynamics during electron cyclotron current drive using hard x-ray measurements in the TCV tokamak, Plasma Physics and Controlled Fusion **62**, 115012 (2020). https://doi.org/10.1088/1361-6587/abb0d3

[4] J. Cazabonne, P. Donnel, S. Coda, J. Decker, G.D. Giannatale et al., Experimental and numerical investigations of electron transport enhancement by electron-cyclotron plasma-wave interaction in tokamaks, Plasma Physics and Controlled Fusion **65**, 104001 (2023). https://doi.org/10.1088/1361-6587/acf39c

[5] Y. Peysson, Transport of fast electrons during LHCD in TS, JET, and ASDEX, Plasma Physics and Controlled Fusion **35**, B253 (1993). https://doi.org/10.1088/0741-3335/35/SB/021

[6] A. Schmidt, P.T. Bonoli, O. Meneghini, R.R. Parker, M. Porkolab et al., Investigation of lower hybrid physics through power modulation experiments on Alcator C-Mod, Physics of Plasmas **18**, 056122 (2011). https://doi.org/10.1063/1.3593112

[7] D. Moreau, the TORE SUPRA Team, Lower-hybrid current drive experiments in TORE SUPRA, Physics of Fluids B: Plasma Physics **4**, 2165 (1992). https://doi.org/10.1063/1.860482

[8] G. Giruzzi, J.L. Ségui, T.D. de Wit, Y. Michelot, Y. Peysson et al., Measurement of the time constants of fast electron distributions in the tore supra tokamak, Phys. Rev. Lett. **74**, 550 (1995). https://doi.org/10.1103/PhysRevLett.74.550

[9] N.J.L. Cardozo, Perturbative transport studies in fusion plasmas, Plasma Physics and Controlled Fusion **37**, 799 (1995). https://doi.org/10.1088/0741-3335/37/8/001

[10] R. Prater, Heating and current drive by electron cyclotron waves, Physics of Plasmas **11**, 2349 (2004). https://doi.org/10.1063/1.1690762

[11] Y. Peysson, D. Mazon, J.F. Artaud, A. Ekedahl, L. Delpech et al., Lower hybrid current drive in high aspect ratio tokamaks, Journal of Fusion Energy **39**, 270 (2020). https://doi.org/10.1007/s10894-020-00266-1

[12] J. Decker, Y. Peysson, J.F. Artaud, E. Nilsson, A. Ekedahl et al., Damping of lower hybrid waves in large spectral gap configurations, Physics of Plasmas **21**, 092504 (2014). https://doi.org/10.1063/1.4894749

[13] Y. Peysson, F. Imbeaux, Tomography of the fast electron bremsstrahlung emission during lower hybrid current drive on TORE SUPRA, Review of Scientific Instruments **70**, 3987 (1999). https://doi.org/10.1063/1.1150025

[14] T. Barbui, L.F. Delgado-Aparicio, Y. Savoye-Peysson, B. Stratton, R. Dumont et al., Versatile multi-energy hard x-ray camera to study confined and unconfined fast electron dynamics and anisotropies, Review of Scientific Instruments **95**, 083539 (2024). https://doi.org/10.1063/5.0219159

[15] S. Gnesin, S. Coda, J. Decker, Y. Peysson, Suprathermal electron studies in the TCV tokamak: Design of a tomographic hard-X-ray spectrometer, Review of Scientific Instruments **79**, 10F504 (2008). https://doi.org/10.1063/1.2957843

[16] G. Giruzzi, M. Zabiégo, T. Gianakon, X. Garbet, A. Cardinali et al., Dynamical modelling of tearing mode stabilization by RF current drive, Nuclear Fusion **39**, 107 (1999). https://doi.org/10.1088/0029-5515/39/1/307

[17] J. Cazabonne, S. Coda, J. Decker, O. Krutkin, U. Kumar et al., Impact of microwave beam scattering by density fluctuations on the electron–cyclotron power deposition profile in tokamaks, Nuclear Fusion **64**, 026019 (2024). https://doi.org/10.1088/1741-4326/ad1af6

[18] Y. Peysson, J. Decker, Numerical simulations of the radio-frequency-driven toroidal current in tokamaks, Fusion Science and Technology **65**, 22 (2014). https://doi.org/10.13182/FST13-643

[19] Y. Peysson, J. Decker, L. Morini, A versatile ray-tracing code for studying rf wave propagation in toroidal magnetized plasmas, Plasma Physics and Controlled Fusion **54**, 045003 (2012). https://doi.org/10.1088/0741-3335/54/4/045003

[20] J. Artaud, F. Imbeaux, J. Garcia, G. Giruzzi, T. Aniel et al., Metis: a fast integrated tokamak modelling tool for scenario design, Nuclear Fusion **58**, 105001 (2018). https://doi.org/10.1088/1741-4326/aad5b1

[21] J. Hillairet, D. Voyer, A. Ekedahl, M. Goniche, M. Kazda et al., ALOHA: an Advanced LOwer Hybrid Antenna coupling code, Nuclear Fusion **50**, 125010 (2010). https://doi.org/10.1088/0029-5515/50/12/125010

[22] J.M. Moret, B.P. Duval, H.B. Le, S. Coda, F. Felici et al., Tokamak equilibrium reconstruction code LIUQE and its real time implementation, Fusion Engineering and Design **91**, 1 (2015). https://doi.org/10.1016/j.fusengdes.2014.09.019

[23] Y. Peysson, J. Decker, Fast electron bremsstrahlung in axisymmetric magnetic configuration, Physics of Plasmas **15**, 092509 (2008). https://doi.org/10.1063/1.2981391